

## **GPR ESTIMATION OF THE GEOMETRICAL FEATURES OF BURIED METALLIC TARGETS IN TESTING CONDITIONS**

**Francesco Soldovieri<sup>1</sup>, Ilaria Catapano<sup>1</sup>,  
Pier Matteo Barone<sup>2</sup>, Sebastian E. Lauro<sup>2</sup>,  
Elisabetta Mattei<sup>2</sup>, Elena Pettinelli<sup>2</sup>, Guido Valerio<sup>3</sup>,  
Davide Comite<sup>4</sup>, and Alessandro Galli<sup>4, \*</sup>**

<sup>1</sup>I.R.E.A., Institute for Electromagnetic Sensing of the Environment, National Research Council of Italy, Via Diocleziano 328, Naples 80127, Italy

<sup>2</sup>Department of Mathematics and Physics, Roma Tre University, Via della Vasca Navale 84, Rome 00146, Italy

<sup>3</sup>I.E.T.R., Institut d'Electronique et de Télécommunications de Rennes, University of Rennes 1, Campus Beaulieu, Avenue du Général Leclerc, Rennes 35042, France

<sup>4</sup>D.I.E.T., Department of Information Engineering, Electronics and Telecommunications, "Sapienza" University of Rome, Via Eudossiana 18, Rome 00184, Italy

**Abstract**—The capability of Ground Penetrating Radar (GPR) systems of accurately reconstructing the geometrical features of buried objects when working in critical conditions is investigated. A customized microwave tomographic approach is used to tackle the imaging through the processing of comparative experimental and synthetic GPR data. The first ones have been gathered in laboratory controlled conditions, while the second ones have been obtained by exploiting an ad-hoc implementation of a CAD tool. Attention is paid to the significant case of 'strong' scatterers having size comparable to the wavelengths of the probing signal, and possibly located close to the interface where the GPR antennas move. The results from imaging point out the potential of the proposed approach, showing in particular to which extent in challenging operational settings, it is possible to recover also the information about the shape of metallic targets in addition to their correct location and size.

---

*Received 5 December 2012, Accepted 27 February 2013, Scheduled 1 March 2013*

\* Corresponding author: Alessandro Galli (galli@diet.uniroma1.it).

## 1. INTRODUCTION AND BACKGROUND

Ground Penetrating Radar (GPR) is a well-assessed tool to provide fast and reliable investigations for subsurface prospecting in a large variety of applications [1, 2]. GPR is often employed for nondestructive testing close to a ground interface with the aim of localizing buried targets in the shallow subsurface, such as in landmine detection and other important civil, forensic, archaeological, geophysical, and planetary applications [1–10].

In particular, GPR has extensively been used for the detection and recognition of metallic objects. Indeed, radar reconstruction can successfully be achieved in various soil and material conditions and for different scatterer dimensions and depths [1, 5, 11–13]. On the other hand, the estimation of the target geometric parameters, such as size and shape, is much more challenging and, to our knowledge, very few papers have tackled this problem [14]. Several authors, for instance, have addressed the problem of pipes or rebar radius estimation [12, 15, 16], however no specific work has been done on the reconstruction of geometrical features.

It should also be emphasized that in order to validate any algorithm of shape reconstruction, it is fundamental to perform a controlled experiment, where both the electromagnetic parameters of the host material and the geometry, dimension, and depth of the metallic targets can be measured with a good accuracy. These conditions are difficult to be achieved in a large test site (see, e.g., [17, 18] and the literature therein) but can be obtained in laboratory scale experiments [14, 19–21].

Many different studies have also explored various types of ‘forward’ GPR scattering problems by means of analytical and numerical approaches [1, 2, 20, 22–25]. Nowadays, the use of Computer Aided Design (CAD) software enables for very flexible and efficient tools providing ‘realistic’ analyses of quite complex GPR scenarios, which nonetheless should require suitable validation through compared experimental evidence. With regards to these issues, useful test cases which can be found in the literature are however rather limited [20].

The reliability and effectiveness of the reconstructed images, providing information on the geometrical features of the objects (i.e., location, size, and shape), depend both on the amount and quality of the GPR data and on the adopted imaging procedures, which are mostly based on the solution of an inverse scattering problem [26]. The imaging algorithms that can be implemented for these applications are extremely various, since efficient ad-hoc procedures are usually searched for in connection with the peculiarities of the scenarios to be

investigated [27–31].

In particular, a good number of methods have been developed to tackle the problem of the shape reconstruction of nonpenetrable objects. A first class of approaches are based on the solution of a nonlinear inverse scattering problem via an iterative minimization scheme [32, 33]. However, due to the nonlinearity of the inverse problem, the solution scheme may suffer of the presence of local minima ('false' solutions) affecting the overall reliability of the reconstruction procedure, and suitable regularization strategies have to be adopted to assure the consistency of the results [34]. Other classes of approaches are those exploiting the definition of 'topological derivative' [35] and the so-called 'qualitative' methods [36]. In particular, among these latter the Linear Sampling Method (LSM) [37, 38] is worthy to be considered since it allows a morphological reconstruction of single or multiple objects (dielectric and/or metallic) from single-frequency scattered-field data, without requiring approximations and a priori information. Unfortunately, LSM can properly work provided that a suitable amount of multi-view and multi-static data are available [39]. This kind of data cannot be gathered with the commonly adopted GPR systems, which allow only multi-monostatic (transmitting antenna, Tx, coincident with the receiving antenna, Rx) or multi-bistatic (Tx antenna separated by a fixed offset from the Rx one) measurement configurations.

In this work, we consider solution schemes based on a simplified model of the electromagnetic scattering such as Kirchhoff approximation [40–43]. Under the Kirchhoff approximation, the reconstruction provides an image corresponding to the support of the induced surface-current distribution on the illuminated region [40–42] and the unknown-to-data mapping is linear. This linear inverse problem is regularized by using the Singular Values Decomposition (SVD) [26]; the absence of local minima favorably affects the reliability of the results and the low computational burden allows us to deal with 'large' (in terms of wavelengths) investigation domains, as the ones considered in the following. A first Kirchhoff-based inverse model for half-space geometry has been presented and analyzed in [44] when the incident field is a plane wave, whereas the case of a multi-monostatic configuration has been dealt with in [45] by considering a homogeneous scenario. Now, by exploiting the concepts in [43–46], we present a Kirchhoff-based inversion scheme in the case of a multi-bistatic configuration and a half-space scenario.

The outlined variety of studies performed on these topics illustrates therefore that the GPR diagnostics is influenced by several factors, mainly concerning the overall operative settings, the quality of

the data of the forward scattering problem, and the adopted inversion procedures. In this frame, our study addresses here such important issues in connection with the following adoptions:

- A complete and efficient technique is searched for GPR detection as regards the features of metallic targets, which involves both location and geometry of the scatterers, with attention to the recovery of the dimensions and also of the shape of buried objects.
- Our tests are concerned with critical functional conditions under which GPR reconstructions are performed. In particular, these are characterized by the investigation of challenging realistic scenarios, where ‘strong’ scatterers are placed in a shallow subsurface and have dimensions comparable to the resolution limits, the Tx/Rx antennas have offsets usually larger than the target depth and also work in near-field regions (instead of far-field ones, as usual in most of the scattering approaches).
- The direct data from measurements are achieved through a tailored laboratory setup of a ‘sand-box’ experiment with control of physical and geometrical parameters. Metallic targets with canonical shapes are buried in a ground medium and a commercial bistatic GPR instrument, moving at the interface, gathers scattered field data. Such realistic measurements also allow us to test the quality of imaging in the presence of noise on data and uncertainties about the background scenario.
- A versatile customized CAD setup is also used for more efficient and accurate comparisons, thus significantly widening the cases of potential interest for GPR applications. This numerical tool is able to deal with quite complex electromagnetic scenarios, accounting for realistic details of the antenna system, of the signal waveforms, of possible dispersive and ohmic effects, of inhomogeneities of the media, etc.. These synthetic data on the scattering can also be reported under the usual B-scan forms.
- A stable and robust approach to the inverse scattering problem is applied through an implementation of a microwave tomographic approach, according to the above-outlined features. As said, this algorithm is able to account for different kinds of configurations (as the multi-bistatic one adopted here) and various environments (e.g., half spaces, layered media, etc.), and here it is specifically designed for strong scatterers, as considered in the following.

Under these assumptions, the imaging results derived from both measured and synthetic data are able to clarify how it is possible to estimate the fundamental geometrical features of the buried scatterers,

not only in terms of accurate location of their depth from interface but also for the geometry of the illuminated part of the target.

The work is organized as follows: Section 2 illustrates the experimental setup for the scattering problem, which involves shallow metallic targets buried in a sandy soil and revealed by a commercial GPR instrument. Section 3 presents the main characteristics of the CAD implementation used as a reference for additional quantitative information on the forward problem. Section 4 describes the distinctive features of the microwave tomographic approach, which faces the imaging as a linear inverse-scattering problem. Section 5 discusses the results of the imaging, assessing the capability of accurate reconstruction of location, size, and shape of different targets, in the frame of the hypotheses and criticalities of the problem. Section 6 outlines some conclusive remarks and further perspectives.

## 2. GPR EXPERIMENTAL SETUP: RESULTS FOR SCATTERING

A laboratory setup was built in order to acquire experimental GPR data to be further processed and inverted. The setup is constituted by a box made of fiberglass, having approximate dimensions  $150 \times 100 \times 30$  cm (length, width, and height, respectively), which can be filled by different background materials. (Additional details can be found in [20], where the same experimental setup was used for different studies.)

In the case at hand, a mixture of synthetic glass beads was chosen as hosting material, which can be regarded as an analogue of a sandy soil [47]. The electromagnetic features of this material, which is nonmagnetic and with negligible losses, were investigated independently through a Time Domain Reflectometry (TDR) analysis [48–50]. Such an analysis allowed us to fix the relative dielectric permittivity of the glass beads equal to 3.2 [20, 50].

Measurements were performed using the commercial GPR device “PulseEkko Pro” by Sensors and Software Inc. [51], equipped with a pair of dipole antennas having a 1 GHz bandwidth around the nominal central frequency of 1 GHz. In the measurements, the GPR antenna system was moved along the length of the box at the soil smooth interface, in a multibistatic configuration having an offset between the Tx/Rx antennas of about 19 cm (center to center). A view of the laboratory experimental setup is given in Fig. 1: in Fig. 1(a), the box with filling medium and scatterers are shown; in Fig. 1(b), the GPR Tx/Rx antennas placed on the ground surface are portrayed.

In order to account for the case of electromagnetic nonpenetrable

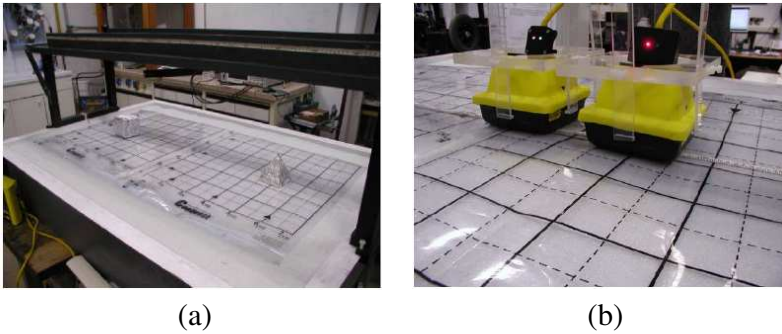


**Figure 1.** View of the GPR laboratory experimental setup: (a) the artificial sand box, filled with a ground medium in which scatterers are buried; (b) the commercial GPR instrument with coupled Tx/Rx antennas for the measurements at the interface.

**Table 1.** Geometry of the objects investigated experimentally.

Object	Geometry
Cube	Side: 9 cm
Sphere	Radius: 8 cm
Cone	Base diameter: 9 cm; height: 10 cm
Pyramid with square basis	Base: $9 \times 9$ ; height: 10 cm
Cylinder	Diameter: 5 cm; height: 10 cm
Parallelepiped with square basis	Base: $5 \times 5$ ; height: 10 cm

(metallic-type) scatterers, GPR measurements were carried out for targets made of hard wood wrapped with aluminum foils. In particular, several targets having canonical geometries and size comparable in terms of typical probing wavelengths were considered. The details of the tested geometries are given in Table 1.

The objects were located at a fixed depth from the air-sand interface, that is  $9(\pm 1)$  cm with respect to the upper face or top point of the metallic targets, according to their geometry.

The raw GPR outcomes are given under the usual form of radar B-scan sections or ‘radargrams’ [1, 2]. These are generated here by transmitting a Gaussian-type pulse from each position along the survey line and collecting the signal scattered by the buried objects from the receiving antenna. As an example, Fig. 2 shows the radargram

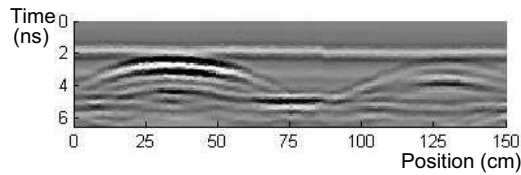


**Figure 2.** Example of a measured GPR radargram in the synthetic sand box. The radar signatures are due to different metallic buried scatterers placed along the major length of the box: a cube (on the left) and a pyramid (on the right). Details on the physical parameters chosen are provided in the main text.

measured when a cube was located on the left of the major length of the box and a square-based pyramid was on the right side at a distance of about 80 cm. In Fig. 2 the effects of different wave contributions appear according to well-established classifications [1, 2]. In particular, the first received event is a ‘direct wave’, which travels straightforwardly from Tx towards Rx antenna. This effect is partly limited by the shielding and by the directional features of the radiators and, when the background has rather homogeneous characteristics, as in the case at hand, it can be dropped out from the output data, with the so-called ‘background removal’ procedure [20]. Such a processing step gives rise to a cleaner pattern focused on the scattering contributions arising from the targets. Further, the roughly-hyperbolic events visible in the radargram of Fig. 2 are produced by the main ‘scattered wave’ and clearly emphasize the presence of the buried objects. It is worth noting a lighter and slightly-delayed hyperbolic event for the pyramid, if compared to the cube response, which is related to the lower scattering cross section of the tip wedge with respect to a flat side. Additional backscattered contributions appearing in Fig. 2 can be associated to the bottom interface of the sand box. In particular, being the box located on two lateral wooden tables and airsuspended in its central part, the reflection effect is particularly visible in the central region due to the strong dielectric contrast occurring between sand and air.

### 3. GPR SIMULATION SETUP: RESULTS FOR SCATTERING

In order to provide further reference GPR data useful for testing the inversion procedure, the scattering problem was simulated by taking advantage of a flexible numerical setup. In particular, the commercial electromagnetic time-domain CAD tool “CST Microwave Studio” [52] was used to simulate scenarios similar to the experimental ones.

In the simulations, an environment made of a two layers was considered. The first layer is made by air, while the second one is given by a dielectric material representing the hosting soil used in the experiments. Accordingly, such a material is nonmagnetic, lossless and has a relative dielectric permittivity equal to 3.2. Moreover, since the irregularities of the sandy interface occurring in the experimental setup are small with respect to the wavelengths of the probing signals and their scattering effects can be certainly neglected when compared to the ones due to the buried metallic scatterers, a flat air-sand interface was simulated. In this environment, perfect electric conductor (PEC) objects (whose geometries have been presented in Table 1) were inserted in locations similar to those considered during the experiments (about 10 cm deep from the interface).

The overall dimensions of the simulated region are 80-cm length, and 50 cm in width and depth. The region is discretized by means of a hexahedral mesh, whose elements have size less than  $\lambda/15$ ,  $\lambda$  being the smaller wavelength in the considered frequency range (0.5–1.5 GHz). Perfect-matched-layer (PML) boundaries conditions have been imposed on the side walls and the bottom of the simulated environment, leading to an ideal absence of reflections (homogenous half spaces). This choice allowed us to efficiently reduce the dimensions of the simulation region and also to focus our attention exclusively on the scattering effects of the buried targets. Therefore, the simulations differ a bit from the experiments, which take also into account the reflection from the bottom of the box. It is anyway worth noting that the simulation tool gives the possibility to consider several and complex scenarios with affordable computational efforts. (Further details on these aspects can be found in [20], where the numerical setup was introduced for other types of analysis.)

In order to acquire simulated data as consistent as possible with the measured ones and then to compare the imaging results obtained in synthetic and experimental conditions, a pair of wide-band printed monopole antennas having bandwidth similar to the nominal one used in the commercial GPR system were designed and simulated. The simulated system is fed at the Tx antenna input with a Gaussian pulse signal having a spectrum between 0.5 and 1.5 GHz (defined among frequencies having 10% of its maximum amplitude) and is generated as the modulation of a pulse through a 1 GHz sinusoid.

The Tx/Rx antennas are placed on the soil surface, sweeping along the longer planar direction with step of 3 cm in a bistatic configuration having a fixed offset of 19 cm, i.e., that occurring in the laboratory measurements. The simulated setup is exemplified in Fig. 3: Fig. 3(a) gives a view of the numerical environment including

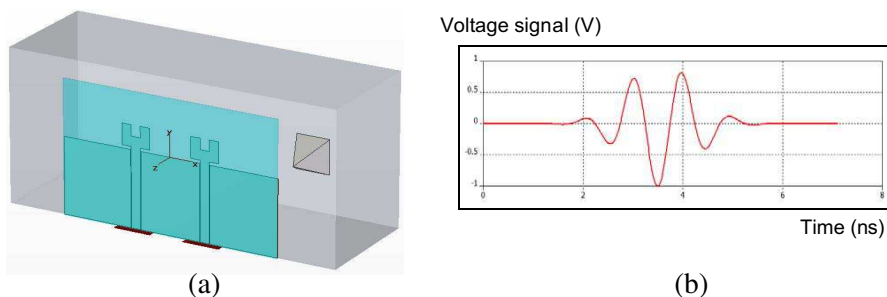


**Figure 3.** The GPR numerical setup based on the CAD tool: (a) view of the simulation environment, including Tx/Rx printed antennas placed on the dielectric medium interface and a buried scatterer; (b) simulated waveform of the GPR transmitted signal.

dielectrics, scatterers, and antenna system; Fig. 3(b) shows a typical simulated waveform of the GPR transmitted signal.

At each position, the Tx antenna radiates a pulse and at the output port of the Rx antenna a signal, including the back-scattered wave from the objects, is gathered. Thus, a grey-scale 2D ‘simulated radargram’ for the investigated domain can also be generated. Suitable signal processing is anyway needed to properly emphasize the scattering effects. In particular, as said, the time-domain output signal is generally made by a first contribution guided by the soil/air interface along the linear path between Tx and Rx antennas. This ‘undesired signal’ (direct wave) is followed at a later time by the ‘useful signal’ (scattered wave) from the buried target. Under the described assumptions, the direct wave can be considered as the same for any position along the observation domain and can be evaluated numerically with a suitable simulation of the Tx/Rx GPR signal performed in the absence of any scattering object. Then, to improve the detectability of the targets by emphasizing the relevant scattering contributions with respect to undesired signals, the direct wave has been subtracted numerically from each collected trace.

An example of a simulated radargram, generated according to the numerical procedure described above, is shown in Fig. 4 for the buried PEC cube with 9-cm side. Specifically, in Fig. 4(a) the result obtained before the background removal is shown. The direct wave is here particularly strong, due to the limited shielding between Tx/Rx antennas in the implementation. The wave scattered by the target produces, indeed, approximately hyperbolic curves partially masked by the direct wave. In Fig. 4(b), the radargram after the background

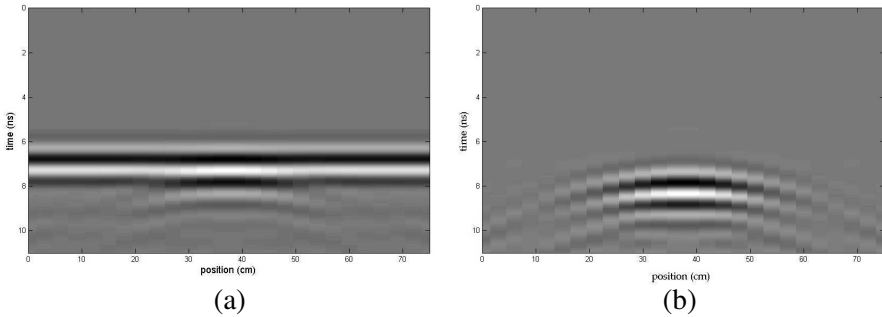


**Figure 4.** GPR radargrams obtained with the simulation setup: (a) complete pattern for a buried PEC cube including direct and reflected waves; (b) pattern for the scattered field after background removal. The geometrical parameters are as in the analogue already considered in the experimental setup (and recalled in the main text).

removal is given. In this figure, only the scattered echo from the cube is present and the top of the diffraction curve is now clearly visible. It is seen that the echoes from the lateral sides of the block are weaker than the echoes from its top. This is an expected outcome, being the scattering from the top of the cube mainly due to strong reflection by a flat interface, while the scattering from the side walls is related to diffracted fields spread over wider angles.

A couple of additional examples of numerical radargrams are presented in Fig. 5. Scattered field patterns, after the removal of the interface contribution, are shown both for a buried PEC sphere in Fig. 5(a) and for a buried PEC pyramid in Fig. 5(b) (see data in Table 1). Comparisons can be made with the relevant radar sections from the previous cases and from measurements. For instance, in Fig. 5(a) it is seen that the sphere, if compared to a cube in a similar situation (Fig. 4(b)), produces a scattered wave with a reduced intensity, as expected; whilst from Fig. 5(b) it is noted that the tip of the pyramid is not well emphasized, in agreement with its reduced reflecting wedge effect.

It is observed that the behaviors of the radargram patterns agree very well with those theoretically expected according to the relevant scattering problem (in terms of amount of reflection, target location, etc.). All these numerical data appear to be pretty ‘regular’ and particularly suitable to be processed by the inversion algorithm as discussed next.

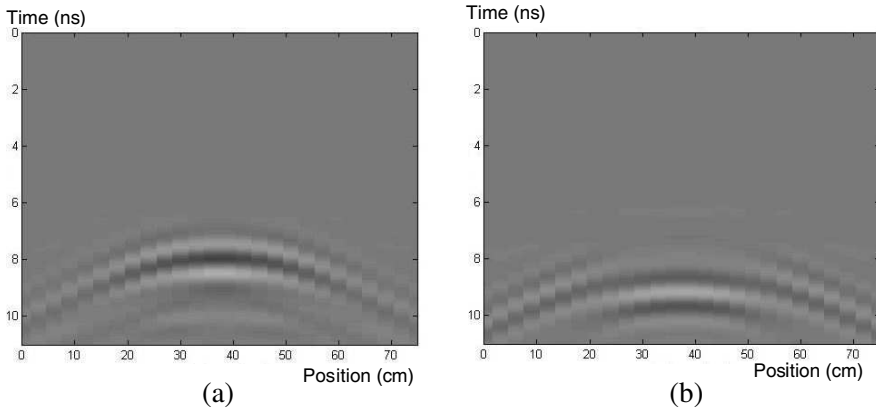


**Figure 5.** GPR scattered-field radargrams obtained through the simulation setup for other canonical shapes of buried scatterers: (a) PEC sphere; (b) PEC pyramid. The geometrical parameters are as in the analogue already considered in the experimental setup (and recalled in the main text).

#### 4. GPR INVERSE PROBLEM VIA A MICROWAVE TOMOGRAPHIC APPROACH

The GPR experimental and numerical data were processed by means of a ‘microwave tomographic approach’ based on the Kirchhoff approximation, which allows us to linearize the inverse scattering problem for metallic (non-penetrable) objects herein considered [42, 46]. As is well known, for the forward problem, i.e., for the evaluation of the scattered field from the known object, the Kirchhoff approximation holds for scatterers whose radius of curvature is large compared to the probing wavelength; on the other hand, when a shape reconstruction problem is faced, it is possible to relax this assumption and a Kirchhoff-based inverse approach is able to give useful information even in the case of objects whose extent is comparable to the probing wavelength [42].

The approach is here formulated for a 2-D geometry as depicted in Fig. 6. The environment is assumed as two homogeneous half-spaces separated by a planar interface ( $z = 0$ , being  $x$  the horizontal scanning axis). In our case, the upper half-space, where the antenna system is located again close to the interface, is air, while the lower half-space represents the medium hosting the objects and it is assumed to have known relative dielectric permittivity  $\varepsilon_b$  and a possible conductivity  $\sigma_b$ . In the following, these parameters are referred to the already presented glass-bead filling material.

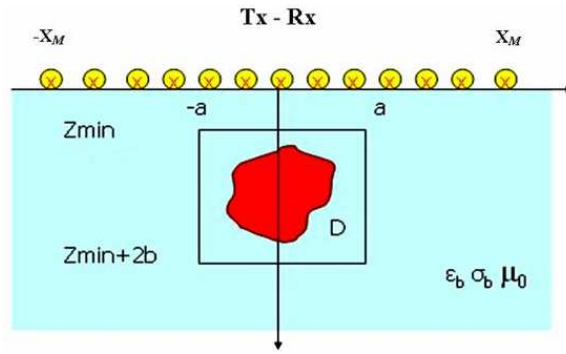


**Figure 6.** Geometry of the 2-D inverse scattering problem according to the microwave tomographic approach.

The incident field source was modelled as time-harmonic (with a typical  $\exp(j\omega t)$  dependence, being  $\omega$  the angular frequency) filamentary electric current, invariant along the horizontal  $y$  axis orthogonal to the investigation  $(x, z)$  plane of Fig. 6. This configuration idealizes the position of the GPR dipole antennas having their major length just oriented along the  $y$ -axis. The data were collected under a multi-frequency multi-bistatic configuration, with the locations of Tx and Rx antennas separated by an offset distance  $\Delta = 19$  cm (as in the laboratory and in the numerical setups). The field was evaluated at discrete frequencies uniformly spaced in the range  $[f_{\min}, f_{\max}]$ . The scattered field was collected by moving the antenna system (Tx/Rx) over a rectilinear observation domain  $x$  at the air/soil interface with the location  $x_s$  of the transmitter ranging from  $-x_M$  to  $x_M$ . The targets to be imaged were enclosed in a priori-known rectangular investigation domain  $D$  in the  $xz$  plane,  $[-a, a] \times [z_{\min}, z_{\max}]$  (see Fig. 6).

Within the above hypotheses, under the Kirchhoff approximation, the scattered field  $E_s$  collected in the upper half-space for  $z = 0$  at each  $\omega$ , when the transmitting antenna is at the source abscissa  $x_s$  and the receiving one is at the observation abscissa  $x_s + \Delta$ , is given as:

$$E_s(x_s, x_s + \Delta) = -j\omega\mu_0 \int_{\Gamma} G(x_s + \Delta, x, z) J_{PO}(x, z, x_s) d\Gamma. \quad (1)$$

In Equation (1),  $\Gamma$  denotes the contour of the scattering object, while  $G(x_s + \Delta, \cdot, \cdot)$  is the ‘external’ Green’s function as evaluated at the point  $(x_s + \Delta, z = 0)$  for the angular frequency  $\omega$ :

$$G(x_s + \Delta, x, z) = -\frac{j}{2\pi} \int_{-\infty}^{+\infty} \frac{e^{-jw_2(u)z}}{w_1(u) + w_2(u)} e^{-ju(x_s + \Delta - x)} du \quad (2)$$

where  $w_i(u) = (k_i^2 - u^2)^{1/2}$ ,  $k_i$  being the wavenumber of the  $i$ -th medium ( $i = 1, 2$ ), and  $u$  the spectral variable along  $x$ . In addition,  $J_{PO}$  is the physical-optics surface current density, evaluated as:

$$J_{PO}(x, z, x_s) = \begin{cases} (2\hat{n}_i \times \mathbf{H}_i(x, z, x_s)) \cdot \hat{i}_y & \text{on } \Gamma_i \\ 0 & \text{on } \Gamma_s \end{cases} \quad (3)$$

where  $\mathbf{H}_i$  is the incident magnetic field in the lower half-space when there are no objects (i.e., the magnetic field transmitted in the lower region),  $\hat{n}_i(x, z) = (n_x(x, z), n_z(x, z))$  is the outward-directed unit vector normal on the scatterer surface at the generic point  $r = (x, z)$ , while  $\Gamma_i$  and  $\Gamma_s$  are the illuminated and shadowed sides of the scatterer, respectively ( $\Gamma = \Gamma_i \cup \Gamma_s$ ). By accounting for the relationship existing among the electric incident field and the magnetic one, the current density  $J_{PO}$  can be expressed as:

$$J_{PO}(x, z, x_s) = \begin{cases} \frac{1}{\pi} \int_{-\infty}^{+\infty} [n_x(x, z)u' + n_z(x, z)w_2(u')] \\ \frac{e^{-jw_2(u')z}}{w_1(u') + w_2(u')} e^{-ju'(x-x_s)} du' & \text{on } \Gamma_i \\ 0 & \text{on } \Gamma_s \end{cases} \quad (4)$$

By replacing Equations (2) and (4) in Equation (1), after some mathematical passages, the scattered field can be rewritten as:

$$E_s(x_s, x_s + \Delta) = -\frac{\omega\mu_0}{2\pi^2} \int_{-\infty}^{+\infty} \frac{e^{ju(x_s+\Delta)}}{w_1(u) + w_2(u)} \int_{-\infty}^{+\infty} \frac{e^{ju'x_s}}{w_1(u') + w_2(u')} \\ \cdot \int_D [n_x(x, z)u' + n_z(x, z)w_2(u')] \delta_\Gamma(x, z) \\ e^{-j[w_2(u')+w_2(u)]z} e^{-j(u'-u)x} dx dz du' du \quad (5)$$

where the quantity  $\delta_\Gamma(x, z)$  denotes a single-layer distribution and allows us to pass from an integral over the contour of the scatterer to the integral over the investigation domain  $D$  [26].

According to the above scattering model, the reconstruction problem is stated as the inversion of the Equation (5), which can be rewritten for all the frequencies belonging to the considered range in a synthetic form as:

$$E_s(x_s, x_s + \Delta, \omega) = L[\gamma]. \quad (6)$$

where the unknown is given by the vector distribution  $\gamma(x, z) = (n_x(x, z), n_z(x, z)) \delta_\Gamma(x, z)$  [46].

Equation (6) states a linear integral relationship between the meaningful signal, i.e., the field scattered by the targets, and the unknown ‘object function’  $\gamma(x, z)$ , which is expressed through the compact operator  $L$  [26, 53].

Being the imaging problem faced as the inversion of the relationship in Equation (6), an ill-posed linear problem must be handled with care through a regularized inversion scheme [53]. A well-known and commonly exploited tool to solve this kind of problems is the truncated singular value decomposition (TSVD) scheme [26, 53]. Accordingly, an approximate stable solution of Equation (6) is given as:

$$\tilde{\gamma} = \sum_{n=0}^N \frac{1}{\sigma_n} \langle \mathbf{E}_s, \mathbf{v}_n \rangle \mathbf{u}_n \quad (7)$$

where  $\{\sigma_n, \mathbf{v}_n, \mathbf{u}_n\}_{n=0}^K$  is the singular system of the matrix  $\mathbf{L}$  (arising from the discretization of the compact operator in Equation (6)),  $\langle \cdot, \cdot \rangle$  denotes the scalar product in the data space,  $K$  denotes the number of measurements, and  $N \leq K$ . The choice of the  $N$  index is performed in order to ensure a trade-off between the contrasting needs for accuracy and resolution from one side (which should push to increase such an index) and for the stability of the solution from the other side (which should push to limit the increase of the index). As result of our inversion approach, we consider the quantity  $|\tilde{\gamma}| = \sqrt{|\tilde{\gamma}_x|^2 + |\tilde{\gamma}_z|^2}$  as the modulus of the vector  $\tilde{\gamma}$  and this is the quantity shown in the reconstructed tomographic images in the next section.

Finally, it is worth nothing that the involved computational time mainly depends on the time needed to fill the matrix  $\mathbf{L}$  and to compute its SVD. Such a time grows up with the number of cells discretizing the investigated domain under test ( $N_{cells}$ ), and in particular, according to [54], the best algorithms for the SVD computation of a  $K \times N_{cells}$  matrix take a time that is proportional to  $O(aK^2N_{cells} + bN_{cells}^3)$ ,  $a$  and  $b$  being constants whose value depends on the adopted algorithm. On the other hand, since the matrix  $\mathbf{L}$  and thus its SVD do not change once the measurement configuration and the features of the investigated domain have been fixed, they can be computed off-line and stored in a databank. In this way, the involved computational time is drastically reduced and real-time results can be achieved.

## 5. RESULTS FOR THE SCATTERERS THROUGH THE INVERSION APPROACH

The reconstruction capabilities of the tomographic approach are investigated by applying the inverse scheme to both the experimental

and simulated data. The results are given in terms of the normalized amplitude of the reconstructed function  $\tilde{\gamma}(\cdot)$  in Equation (7) with respect to its maximum inside the investigation domain  $D$ . It should be reminded that the tomographic reconstructions here manage critical cases of nonpenetrable objects with data gathered under a reflection-measurement configuration, hence most of the information achievable is expected relating to the upper illuminated parts of the reflectors that give rise to the main scattering effects. Accordingly, only the upper side of the objects is expected to be actually well retrieved.

The relevant inversion results are presented separately, starting from the simulation setup (Section 5.1), for which a larger and various set of useful data was derived, and then for the experimental setup (Section 5.2).

### 5.1. Inversion with Simulated Data

According to the simulated environment, the investigated domain is in the lower half-space and its half-size along the longitudinal  $x$  axis is equal to  $a = 40$  cm (80 cm overall), while its extent along the depth ranges from  $z_{\min} = 1$  cm to  $z_{\max} = 50$  cm.

The measurement configuration assumes a bistatic modality with source and receiver separated, as said, by an offset  $\Delta = 19$  cm. The antenna system is moved along the air-soil interface at 25 spatial points with a uniform step of 3 cm. In particular, the Tx antenna moves between  $[-40, 40]$  cm, whereas the Rx antenna moves within  $[-21, 59]$  cm. The working frequency ranges between  $f_{\min} = 0.5$  GHz and  $f_{\max} = 1.5$  GHz with 41 discrete frequencies spaced of 25 MHz. The inversion is regularized by the TSVD approach, where the TSVD index  $N$  is chosen to retain in the summation (7) the singular values larger than 0.1 times the highest singular value.

The first set of results accounts for three buried PEC cubes having different sizes in the simulations (5 cm, 9 cm, and 13 cm) and upper side at depth of 10 cm. Their center is laterally shifted of about 7.5 cm along  $x$  with respect to the center of the investigated domain. The color-plot reconstructions of the ‘object function’, i.e., the tomographic images, are shown in Figs. 7(a), (b), and (c) for the three cube sizes, respectively. In these figures, as in the following ones, the black lines represent the contour of the actual objects.

The results of Figs. 7(a)–(c) corroborate that, despite the relevant wavelengths of the signal in the hosting medium are in the range around 15 cm (i.e., actually comparable to the typical dimensions of our scatterers), accurate images are obtained. From Figs. 7(a)–(c) it is seen that the extents of the upper sides are reconstructed with good accuracy, and this feature is more evident for the larger cubes.

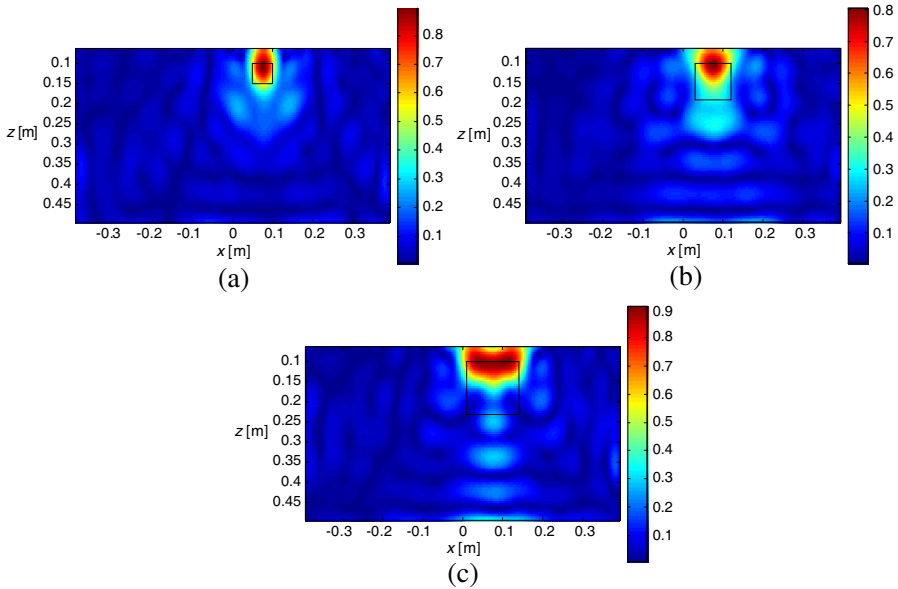


**Figure 7.** Tomographic reconstruction from simulations of three PEC cubes having different sizes (the upper side of the object is at 10 cm depth from the interface): (a) ‘small’ cube with side 5 cm; (b) ‘middle’ cube with side 9 cm; (c) ‘large’ cube with side 13 cm. Other physical parameters are given in the text.

Moreover, the main vertical position is properly localized by the peak values of the TSVD reconstructed function. The thickness of the spot along the depth is due to the finite working frequency and is anyway comparable to the ideal resolution limits, given by  $c_0/2B\sqrt{\epsilon_b} = 8.4$  cm, being  $B = 1$  GHz the signal bandwidth.

The second set of results concerns two other metallic targets previously introduced: a parallelepiped with length 10 cm and square section with side 5 cm, and a cylinder of the same length and diameter 5 cm, both the objects being 10-cm deep. The two targets are placed with their axis parallel to the scanning  $x$  direction. Fig. 8 shows the tomographic reconstructions of the parallelepiped (Fig. 8(a)) and of the cylinder (Fig. 8(b)). Again, the object function describes quite well the location and size of these scatterers.

The third considered numerical data-set is referred to pyramidal and conical metallic targets. Both targets have the same height (10 cm); the pyramid has a square basis with side 9 cm, and the diameter of the conical basis is 9 cm (see Table 1); the axis of both targets is placed vertically. Fig. 9 gives the tomographic reconstruction

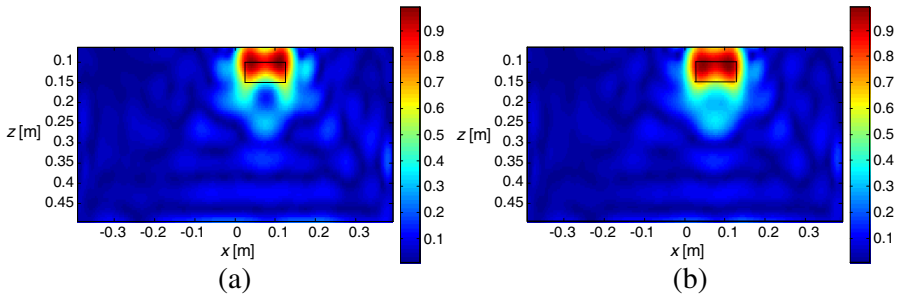


**Figure 8.** Tomographic reconstruction from simulations of buried PEC parallelepiped and cylinder, placed with their major length along the scanning  $x$  direction: (a) parallelepiped; (b) cylinder. Other physical parameters in the text.

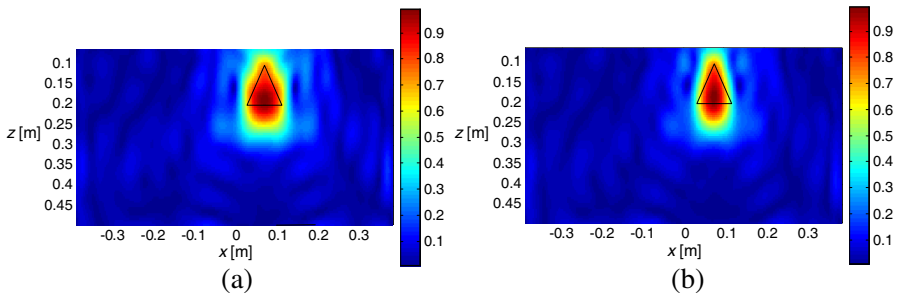


**Figure 9.** Tomographic reconstruction of PEC pyramid and cone from simulations: (a) pyramid; (b) cone. Other physical parameters in the text.

of the pyramid (Fig. 9(a)) and of the cone (Fig. 9(b)). It is interesting to note that the reconstructions are very similar one the other, according to the features of the two shapes in the imaged slice. In particular, the main contribution of the object function appears to be placed slightly below with respect to the upper edge, due to the reduced scattering effect of the wedge shape.

## 5.2. Inversion with Experimental Data

The tomographic approach has also been applied to experimental datasets as detailed in Section 2. Also in this case, the inversion model is concerned with an investigation domain similar to that already presented. Again, the measurement configuration assumes a bistatic modality with the source and receiver separated by 19 cm, spanning in the range  $[-70, 70]$  cm. The antenna system sweeps along the air-soil

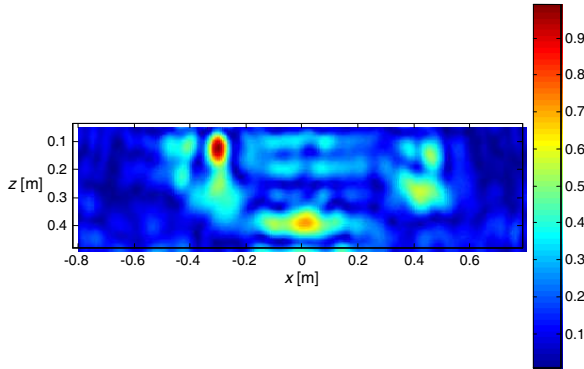


**Figure 10.** Tomographic reconstruction of targets from experimental data for metallic cube and pyramid buried in a sandy soil, as in Fig. 2. Other physical parameters in the text.

interface at 61 spatial points with a step of 2 cm. In particular, the Tx antenna moves between  $[-69.5, 50.5]$  cm, whereas the Rx antenna moves within  $[-50.5, 69.5]$  cm. The working frequency ranges between  $f_{\min} = 0.3$  GHz and  $f_{\max} = 1.3$  GHz, with 26 frequencies spaced of 40 MHz (this slightly-modified frequency range is related to the specific evaluation of the effective spectrum of the signal transmitted by the GPR instrument when positioned on the ground-medium surface).

The first tomographic reconstruction from measured data is shown in Fig. 10 and is referred to the case of a pair of metallic targets already presented in Fig. 2, with a cube (9-cm side) and a pyramid (10-cm height and 9-cm side square basis), both located at a depth of 9 cm (for the top parts) and spaced side by side along  $x$  axis of 80 cm. From this figure, one can observe a spot at about  $x = -30$  cm, which correctly accounts for the upper side of the cube and provides a good estimation of the major reflecting side. The spot at the center of the investigation domain (around  $x = 0$ ), at depth of about 30 cm, is concerned with the reflection from the bottom of the dielectric box (as already emphasized in the radargram of Fig. 2). Finally, the spots at about  $x = 50$  cm are concerned with the location of the main reflecting areas of the pyramid shape.

A further inversion result from measurements refers to the case of parallelepiped and cylinder targets, whose dimensions were already presented in Section 2. The scatterers were placed in this case with their major length perpendicular to the scanning direction, and again spaced along the  $x$  axis of about 80 cm and 9 cm deep. The relevant tomographic reconstruction is presented in Fig. 11. As in the previous case, the main features of the probed scenario can be enlightened

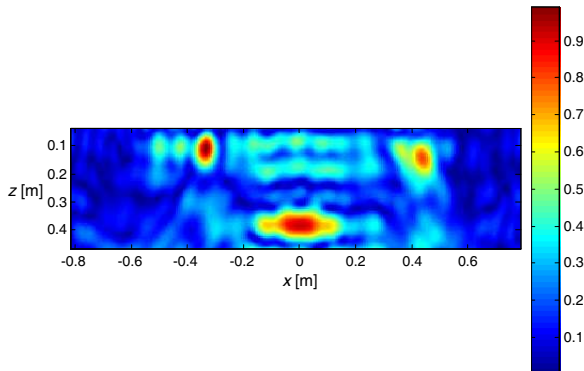


**Figure 11.** Tomographic reconstruction of targets from experimental data for a metallic parallelepiped and a cylinder buried in a sandy soil, with their major lengths perpendicular to the scanning direction. Other physical parameters in the text.

from the tomographic reconstruction. The stronger spot at about  $x = -30$  cm accounts for the upper side of the parallelepiped. As above, the wider spot at the center of the investigation domain is concerned with the bottom of the box. Finally, the spot at about  $x = 50$  cm is concerned with the proper cylinder location, whose scattering effect is correctly less strong than that arising from the parallelepiped (the former presenting a round contour instead of a flat face and edges).

## 6. CONCLUSION

The performance achievable by means of typical GPR systems in connection with an inverse tomographic algorithm was investigated in terms of geometrical characterization of metallic targets buried in a ground medium for testing operation.

An efficient inversion technique was applied by processing direct ad-hoc data on radargrams from both measurements and simulations. Most of the investigations were performed in challenging practical conditions, with nonpenetrable scatterers placed in the near-field region of shallow subsurface and with dimensions comparable to the typical wavelengths of the GPR signals.

The obtained results on imaging showed a very good capability of proving a correct spatial localization of the targets, in conjunction with a satisfactory prediction of the size and shape of their upper side. This has been observed even for realistic measurements in the presence of noise on data and uncertainties about the background scenario.

Intrinsic limits related to the adopted measurement configurations and the finite range of frequencies of the signal spectrum do not anyway allow for the identification of finer geometrical details.

Although our study was devoted here to the analysis of metallic scatterers, it will be interesting to check the potential of this approach also in the cases of electromagnetic penetrable targets (dielectric objects with possible ohmic losses) or for other more complex scenarios (multilayered media, irregular interfaces, etc.), which could significantly enlarge the areas of application related to the GPR technique.

## ACKNOWLEDGMENT

The Authors gratefully acknowledge financial support from the Italian Space Agency through contract ASI n. I/060/10/0 EXOMARS SCIENCE phase C2/D.

## REFERENCES

1. Daniels, D. J. (ed.), *Ground Penetrating Radar*, 2nd edition, The Institution of Electrical Engineers (IEE), London, UK, 2004.
2. Jol, H. M. (ed.), *Ground Penetrating Radar: Theory and Applications*, Elsevier, Amsterdam, The Netherlands, 2009.
3. Cook, J., "Radar transparencies of mine and tunnel rocks," *Geophysics*, Vol. 40, No. 5, 865–885, Oct. 1975.
4. Conyers, L. B., *Ground-penetrating Radar for Archaeology*, AltaMira Press, Walnut Creek, CA, USA, 2004.
5. Pettinelli, E., A. Di Matteo, E. Mattei, L. Crocco, F. Soldovieri, J. D. Redman, and A. P. Annan, "GPR Response from buried pipes: Measurement on field site and tomographic reconstructions," *IEEE Trans. on Geosci. Remote Sens.*, Vol. 47, No. 8, 2639–2645, Aug. 2009.
6. Picardi G., J. J. Plaut, D. Biccari, O. Bombaci, D. Calabrese, M. Cartacci, A. Cicchetti, S. M. Clifford, P. Edenhofer, W. M. Farrell, C. Federico, A. Frigeri, D. A. Gurnett, T. Hagfors, E. Heggy, A. Herique, R. L. Huff, A. B. Ivanov, W. T. K. Johnson, R. L. Jordan, D. L. Kirchner, W. Kofman, C. J. Leuschen, E. Nielsen, R. Orosei, E. Pettinelli, R. J. Phillips, D. Plettemeier, A. Safaeinili, R. Seu, E. R. Stofan, G. Vannaroni, T. R. Watters, and E. Zampolini, "Radar soundings of the subsurface of Mars," *Science*, Vol. 310, No. 5756, 1925–1928, Dec. 2005.

7. Vannaroni, G., E. Pettinelli, C. Ottonello, A. Cereti, G. Della Monica, D. Del Vento, A. M. Di Lellis, R. Di Maio, R. Filippini, A. Galli, A. Menghini, R. Orosei, S. Orsini, S. Pagnan, F. Paolucci, A. R. Pisani, G. Schettini, M. Storini, and G. Tacconi, "MUSES: Multi-sensor soil electromagnetic sounding," *Planetary Space Sci.*, Vol. 52, 67–78, 2004.
8. Pettinelli, E., P. Burghignoli, A. R. Pisani, F. Ticconi, A. Galli, G. Vannaroni, and F. Bella, "Electromagnetic propagation of GPR signals in Martian subsurface scenarios including material losses and scattering," *IEEE Trans. on Geosci. Remote Sens.*, Vol. 45, 1271–1281, May 2007.
9. Ciarletti, V., C. Corbel, D. Plettemeier, P. Cais, S. M. Clifford, and S.-E. Hamran, "WISDOM GPR designed for shallow and high-resolution sounding of the Martian subsurface," *Proc. IEEE*, Vol. 99, No. 5, 824–836, 2011.
10. Turk, A. S., A. K. Hocaoglu, and A. A. Vertiy, Eds., *Subsurface Sensing*, Wiley, Hoboken, NJ, USA, 2011.
11. Yamaguchi, Y., M. Mitsumoto, M. Sengoku, and T. Abe, "Synthetic aperture FM-CW radar applied to the detection of objects buried in snowpack," *IEEE Trans. on Geosci. Remote Sens.*, Vol. 32, No. 1, 11–18, Jan. 1994.
12. Chang, C. W., C. H. Lin, and H. S. Lien, "Measurement radius of reinforcing steel bar in concrete using digital image GPR," *Construction Building Materials*, Vol. 23, No. 2, 1057–1063, Feb. 2009.
13. Arcone, S., D. Finnegan, and G. Boitnott, "GPR characterization of a lacustrine UXO site," *Geophysics*, Vol. 75, No. 4, WA221–WA229, Jul. 2010.
14. Radzevicius, S., "Practical 3-D migration and visualization for accurate imaging of complex geometries with GPR," *J. Environ. Engin. Geophysics*, Vol. 13, No. 2, 99–112, Jun. 2008.
15. Shihab, S. and W. Al-Nuaimy, "Radius estimation for cylindrical objects detected by ground penetrating radar," *Subsurface Sensing Technol. Applicat.*, Vol. 6, No. 2, 151–166, Apr. 2005.
16. Gantala, G., C. V. Krishnamurthy, K. Balasubramaniam, and N. Ganesan, "Shape reconstruction of metal pipes with corrosion defects using single frequency limited view scattered data," *NDT & E Internat.*, Vol. 52, 129–135, Nov. 2012.
17. Grandjean, G., J. C. Gourry, and A. Bitri, "Evaluation of GPR techniques for civil-engineering applications: Study on a test site," *J. Applied Geophysics*, Vol. 45, No. 3, 141–156, Oct. 2000.

18. Zeng, X. and G. A. McMechan, "GPR characterization of buried tanks and pipes," *Geophysics*, Vol. 62, No. 3, 797–806, Jun. 1997.
19. Duchene, B., A. Joisel, and M. Lambert, "Nonlinear inversions of immersed objects using laboratory-controlled data," *Inverse Problems*, Vol. 20, No. 6, S81–S98, 2004.
20. Valerio, G., A. Galli, P. M. Barone, S. E. Lauro, E. Mattei, and E. Pettinelli, "GPR detectability of rocks in a Martian-like shallow subsoil: A numerical approach," *Planetary Space Sci.*, Vol. 62, 31–40, 2012.
21. Ko, K. H., G. Jang, K. Park, and K. Kim, "GPR-based landmine detection and identification using multiple features," *Int. J. Antennas Propag.*, Vol. 2012, Article ID 826404, 7, 2012.
22. Baum, C. E., Ed., *Detection and Identification of Visually Obscured Targets*, Taylor and Francis, Philadelphia, PA, 1999.
23. Uduwawala, D., M. Norgren, P. Fuks, and A. Gunawardena, "A complete FDTD simulation of a real GPR antenna system operating above lossy and dispersive grounds," *Progress In Electromagnetics Research*, Vol. 50, 209–229, 2005.
24. Ozdemir, C., S. Demirci, and E. Yigit, "Practical algorithms to focus B-scan GPR images: Theory and application to real data," *Progress In Electromagnetics Research B*, Vol. 6, 109–122, 2008.
25. Song, L.-P., Q. H. Liu, F. Li, and Z. Q. Zhang, "Reconstruction of three-dimensional objects in layered media: Numerical experiments," *IEEE Trans. on Antennas and Propag.*, Vol. 53, No. 4, 1556–1561, Apr. 2005.
26. Bertero, M. and P. Boccacci, *Introduction to Inverse Problems in Imaging*, Institute of Physics Publishing, London, UK, 1998.
27. Witten, A. J., J. E. Molyneux, and J. E. Nyquist, "Ground penetrating radar tomography: Algorithms and case studies," *IEEE Trans. on Geosci. Remote Sens.*, Vol. 32, No. 2, 461–467, Mar. 1994.
28. Capineri, L., P. Grande, and J. A. G. Temple, "Advanced image-processing technique for real-time interpretation of ground-penetrating radar images," *Int. J. Imaging Systems Tech.*, Vol. 9, No. 1, 51–59, Dec. 1998.
29. Wu, Z. and C. Liu, "An image reconstruction method using GPR data," *IEEE Trans. on Geosci. Remote Sens.*, Vol. 37, No. 1, 327–334, Jan. 1999.
30. Caorsi, S., A. Massa, and M. Pastorino, "A computational technique based on a real-coded genetic algorithm for microwave imaging purposes," *IEEE Trans. on Geosci. Remote Sens.*,

- Vol. 38, No. 4, 1697–1708, Jul. 2000.
31. Hansen, T. B. and P. M. Johansen, “Inversion scheme for ground penetrating radar that takes into account the planar air-soil interface,” *IEEE Trans. on Geosci. Remote Sens.*, Vol. 38, No. 1, 496–506, Jan. 2000.
  32. Kleinman, R. E. and P. M. van den Berg, “Two-dimensional location and shape reconstruction,” *Radio Sci.*, Vol. 29, No. 4, 1157–1169, 1994.
  33. Dorn, O., E. L. Miller, and C. M. Rappaport, “A shape reconstruction method for electromagnetic tomography using adjoint fields and level sets,” *Inverse Problems*, Vol. 16, No. 5, 1119–1156, Oct. 2000.
  34. Catapano, I., L. Crocco, and T. Isernia, “A simple two-dimensional inversion technique for imaging homogeneous targets in stratified media,” *Radio Sci.*, Vol. 39, No. 14, Feb. 2004.
  35. Feijoo, G. R., “A new method in inverse scattering based on topological derivative,” *Inverse Problems*, Vol. 20, No. 6, 1819–1840, Dec. 2004.
  36. Cakoni, F. and D. Colton, *Qualitative Methods in Inverse Scattering Theory*, Springer-Verlag, Berlin, Germany, 2006.
  37. Monk, P., D. Colton, and K. Giebermann, “A regularized sampling method for solving three dimensional inverse scattering problems,” *SIAM J. Sci. Comput.*, Vol. 21, 2316–2330, 2000.
  38. Catapano, I., L. Crocco, and T. Isernia, “On simple methods for shape reconstruction of unknown scatterers,” *IEEE Trans. on Antennas and Propag.*, Vol. 55, 1431–1436, 2007.
  39. Catapano, I., F. Soldovieri, and L. Crocco, “On the feasibility of the linear sampling method for 3D GPR surveys,” *Progress In Electromagnetics Research*, Vol. 118, 185–203, 2011.
  40. Marklein, R., K. J. Langenberg, K. Mayer, J. Miao, A. Shlivinski, A. Zimmer, W. Müller, V. Schmitz, C. Kohl, and U. Mletzko, “Recent applications and advances of numerical modeling and wavefield inversion in nondestructive testing,” *Adv. Radio Sci.*, Vol. 3, 167–174, 2005.
  41. Pierri, R., A. Liseno, and F. Soldovieri, “Shape reconstruction from PO multifrequency scattered fields via the singular value decomposition approach,” *IEEE Trans. on Antennas and Propag.*, Vol. 49, No. 9, 1333–1343, Sep. 2001.
  42. Pierri, R., A. Liseno, R. Solimene, and F. Soldovieri, “Beyond physical optics SVD shape reconstruction of metallic cylinders,” *IEEE Trans. on Antennas and Propag.*, Vol. 54, No. 2, 655–665,

- Feb. 2006.
43. Liseno, A., F. Soldovieri, and R. Pierri, "Improving a shape reconstruction algorithm with thresholds and multi-view data," *Int. J. Electron. Commun.*, Vol. 58, No. 2, 118–124, Mar.–Apr. 2004.
  44. Liseno, A., F. Tartaglione, and F. Soldovieri, "Shape reconstruction of 2-D buried objects under a Kirchhoff approximation," *IEEE Geosci. Remote Sens. Letters*, Vol. 1, No. 2, 118–121, Apr. 2004.
  45. Soldovieri, F., A. Brancaccio, G. Prisco, G. Leone, and R. Pierri, "A Kirchhoff-based shape reconstruction algorithm for the multimonostatic configuration: The realistic case of buried pipes," *IEEE Trans. on Geosci. Remote Sens.*, Vol. 46, No. 10, 3031–3038, Oct. 2008.
  46. Solimene, R., A. Buonanno, F. Soldovieri, and R. Pierri, "Physical optics imaging of 3D PEC objects: Vector and multipolarized approaches," *IEEE Trans. on Geosci. Remote Sens.*, Vol. 48, No. 4, 1799–1808, Apr. 2010.
  47. Robinson, D. A. and S. P. Friedman, "The effective permittivity of dense packing of glass beads, quartz sand and their mixtures immersed in different dielectric backgrounds," *J. Non-Crystalline Solids*, Vol. 305, No. 1–3, 261–267, Jul. 2002.
  48. Topp, G. C., J. L. Davis, and A. P. Annan, "Electromagnetic determination of soil water content: Measurements in coaxial transmission lines," *Water Resources Res.*, Vol. 16, 574–582, Mar. 1980.
  49. Pettinelli, E., A. Cereti, A. Galli, and F. Bella, "Time domain reflectometry: Calibration techniques for accurate measurement of dielectric properties of various materials," *Rev. Sci. Instrum.*, Vol. 73, 3553–3562, 2002.
  50. Mattei, E., A. De Santis, A. Di Matteo, E. Pettinelli, and G. Vanaroni, "Time-domain reflectometry of glass beads/magnetite mixtures: A time and frequency domain study," *Applied Physics Lett.*, Vol. 86, No. 22, 224102-3, May 2005.
  51. *PulseEkko Pro User Guide*, Sensors and Software, Inc., Canada, 2006.
  52. *CST Microwave Studio Manual*, CST, Germany, 2002.
  53. Tikhonov, A. N. and V. Y. Arsenin, *Solution of Ill-Posed Problems*, Winston and Wiley, Washington, DC, USA, 1977.
  54. Golub, G. H. and C. F. van Loan, *Matrix Computations*, 3rd edition, Johns Hopkins Univ. Press, Baltimore, MD, USA, 1996.